machines

MDPI

Article

Mathematical Validation of Experimentally Optimised Parameters Used in a Vibration-Based Machine-Learning Model for Fault Diagnosis in Rotating Machines

Natalia Espinoza Sepulveda and Jyoti Sinha *

Dynamics Laboratory, Department of MACE, The University of Manchester, Manchester M13 9PL, UK; natalia.espinozasepulveda@manchester.ac.uk
* Correspondence: jyoti.sinha@manchester.ac.uk

Abstract: Mathematical models have been widely used in the study of rotating machines. Their application in dynamics has eased further research since they can avoid time-consuming and exorbitant experimental processes to simulate different faults. The earlier vibration-based machine-learning (VML) model for fault diagnosis in rotating machines was developed by optimising the vibration-based parameters from experimental data on a rig. Therefore, a mathematical model based on the finite-element (FE) method is created for the experimental rig, to simulate several rotor-related faults. The generated vibration responses in the FE model are then used to validate the earlier developed fault diagnosis model and the optimised parameters. The obtained results suggest the correctness of the selected parameters to characterise the dynamics of the machine to identify faults. These promising results provide the possibility of implementing the VML model in real industrial systems.

Keywords: rotating machine; rotor faults; fault diagnosis; finite-element model; mathematical simulation; machine learning

Citation: Sepulveda, N.E.; Sinha, J. Mathematical Validation of Experimentally Optimised Parameters used in Vibration-Based Machine-Learning Model for the Faults Diagnosis in Rotating Machines. *Machines* **2021**, *9*, 155. https://doi.org/10.3390/machines9080155

Academic Editors: Hui Ma and Davide Astolfi

Received: 29 June 2021
Accepted: 3 August 2021
Published: 7 August 2021

1. Introduction

Mathematical models are a valuable tool used in the study of rotating machines. They are commonly implemented with the aim of understanding the dynamic responses of such machines under certain conditions, especially in the presence of rotor faults or defects. In addition to enhancing the understanding of the machine behaviour, mathematical models ease data generation to conduct further studies, which may be difficult to obtain through experimental setups. Rotor defects have been widely simulated in mathematical models, the Jeffcott Rotor and the Finite-Element (FE) method being among the most commonly used techniques.

It is possible to identify, in the literature, the study of complex dynamic rotor behaviours by means of simple rotor-bearing models. Nonlinear vibrations were investigated in a simple bladed rotor with contact occurring due to misalignment [1]. Here, the developed Jeffcott model with elastic blades is compared against experimental results, finding the model to be applicable to rotors running at under-critical speed, for example hydropower rotors. Vlajic et al. [2] investigated the contact in a modified Jeffcott rotor, which includes torsional and lateral responses. Two approaches regarding friction are taken into account to simulate the contact effect, suggesting its application in systems with large torsional deformations. Impacts between a planar rotor with unbalance and an outer snubber ring were investigated by Paez Chavez et al. [3]. They used a Jeffcott rotor model and validated it through experiments at different speeds, identifying sequences of dynamic scenarios.

Guo et al. [4] studied the dynamic behaviour of the Jeffcott rotor in the presence of a transverse breathing crack in the vicinity of a rigid disc, identifying a unique crack vibration signature at 2× and 3× superharmonics through empirical mode decomposition method (EMD). Further validation of the theoretical study was conducted in an experimental rotor testbed with a real fatigue crack [5], finding the method to be reliable and practical. Gomez et al. [6] studied the energy changes in a rotor with crack, applying wavelet transform theory over analytically created data in a Jeffcott rotor. Increasing 1×, 2×, and 3× energy levels were found in the presence of the defect; however, in experimental investigations carried out at different steady speeds and crack depths, only the 3× component resulted in a fault indicator.

Singh and Rajiv [7] also studied breathing cracks in a rotor, but including active magnetic bearings in supports. They used the Jeffcott rotor with an offset disc, and developed an algorithm that allows the identification of the crack, as well as to estimate other model parameters, such as damping, unbalance, and constants due the supports. The study developed by Heindel et al. [8] included active bearings in a Jeffcott rotor as well, proving their ability to eliminate bearing forces and resonance when the machine is subject to unbalance. Eissa and Saeed [9] studied a horizontally supported Jeffcott rotor system, proposing a controller for the nonlinear vibrations, which results into a reduction in oscillation amplitude.

More complex machine configurations are found to be studied through FE models. Extensive research in blade-casing rub in aeroengines have been carried out. Chen [10] included in their model the number of blades and geometrical considerations due relative to rotor–stator position. This model was designed to assess different rubbing conditions, and its generated responses were validated in an experimental rig. Hong et al. [11] developed a FE model of an experimental rig of an aeroengine. Structural effects in the blades, such as deformation and stress, were studied by means of the numerical method. Regarding the consistency between experimental and numerical results, the model is proposed to be used for design and analyses purposes.

Wang et al. [12] worked to predict the transient dynamic response of dual rotor blade-casing system with blade off in a turbofan engine through a multi-bearing FE model. Here, rub arises as an effect of the asymmetry after missing the blade, and sudden imbalance leads to impact loads. The study reveals the big impact that inertia asymmetry has in the transient responses of the machine.

Guo et al. [13] simulated the rub between rotating blade and flexible casing. They proposed a clamped blade model, with the flexible casing simulated as a cylindrical shell. The vibration responses obtained in the developed models are compared against the results from the FE model. Zeng et al. [14] studied rub in a single blade-casing system with flexible supports by an (FE) model of two-node Timoshenko beam, and programming two types of algorithm for the contact interface. Different to most of the approaches in the literature, Mokhtar et al. [15] studied rub considering a coupled rotor–stator system. This model attempts to provide a realistic dynamic interaction among the components, which are considered to be coupled through bearing supports. Vibrations in stator are studied to identify the presence of rub.

Xiang et al. studied coupled faults of crack, rub-impact, and oil–film instability [16–18]. A simple mathematical model, consistent in shaft, disc, and two bearings as supports, is proposed, where effects of shear, torsional vibration, and gyroscopic couple were neglected. It is found that rotor stability is affected by stator stiffness and crack depth; furthermore, a strong nonlinearity is observed at high speed. Theoretical results are consistent with experimental validations. Wang et al. [19] worked on the unbalancing effects on the nonlinear dynamics in cracked rotors. A 3D FE model of a simple rotor with a breathing crack is considered. The study showed the significant contributions of unbalance to the breath mechanism of the crack and, therefore, to the rotor dynamics.

This brief literature review has exposed how mathematical models have contributed to different investigations in the field of rotating machines. In this particular study, a FE

model of an experimental rig is presented. Several rotor-related faults, such as misalignment, shaft bow, looseness in pedestal and rotor rub, alongside the healthy condition, are simulated. Vibration responses are generated in the FE model to validate a smart vibration-based machine-learning fault diagnosis model earlier developed using experimental vibration data. The paper includes the details of experimental rigs and data, a summary of the earlier proposed VML fault diagnosis model, the FE model of the experimental rig, and the results obtained in the validation.

2. Experimental Rig and Data

2.1. Experimental Rig and Mode Shapes

Existing vibration data collected from an experimental rig [20] are used in the parameter optimisation study [21]. The experimental setup of the rig is shown in Figure 1a. The schematic of the rig in Figure 1b shows all the main components, which are also included in the finite-element model developed in further sections of this paper.

The rig consists of two shafts, Sh1 and Sh2, with a length of 1.0 m and 0.5 m, respectively. Both are coupled by a rigid coupling, C2, and rest on 4 ball bearings, B1 to B4, mounted on four flexible pedestals, P1 to P4. Balancing discs D1 and D2 are mounted on Sh1, while D3 is on Sh2. The rig is driven by an electric motor, connected to Sh1 by a flexible coupling, C1, which is used in order to avoid the transmission of vibration from the motor to the rotor. The steel base acts as foundation of the machine. Locations a1 to a9 in Figures 1 and 2 represent the measurement locations used in the modal test, where natural frequencies and mode shape were obtained [20]. The natural frequencies of the rig are 50.66 Hz, 56.76 Hz, 59.2 Hz, and 127 Hz. Figure 2 has the first 2 mode shapes of the experimental rig [20].

(a)

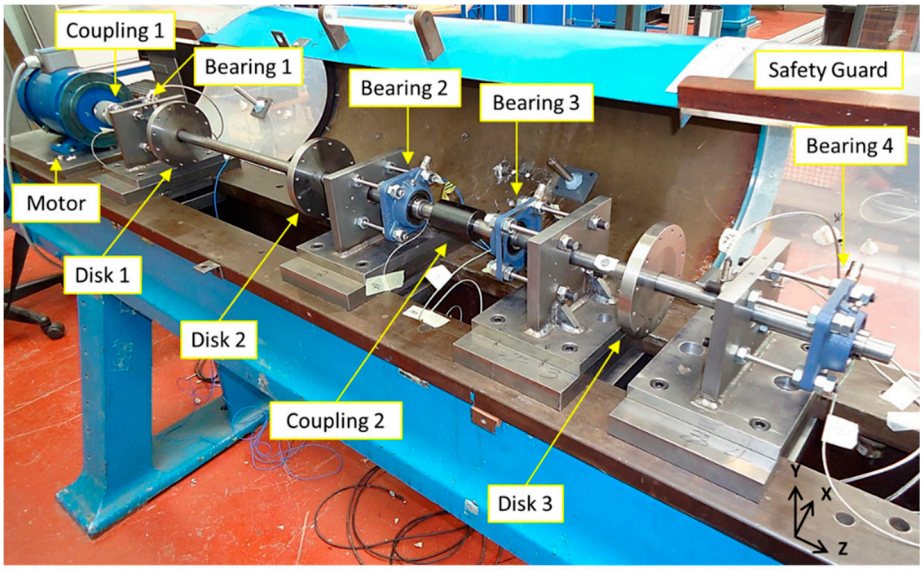

(b)

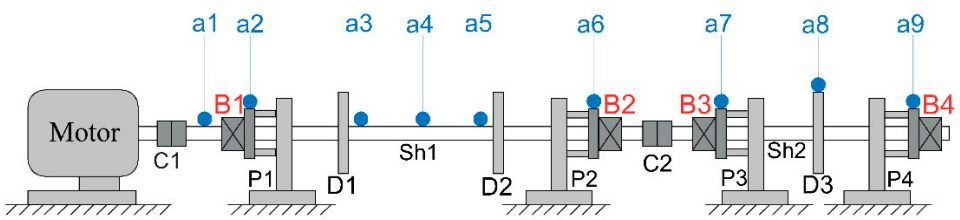

Figure 1. Experimental rig. (**a**) Experimental setup [20]; (**b**) Schematic of the experimental rig.

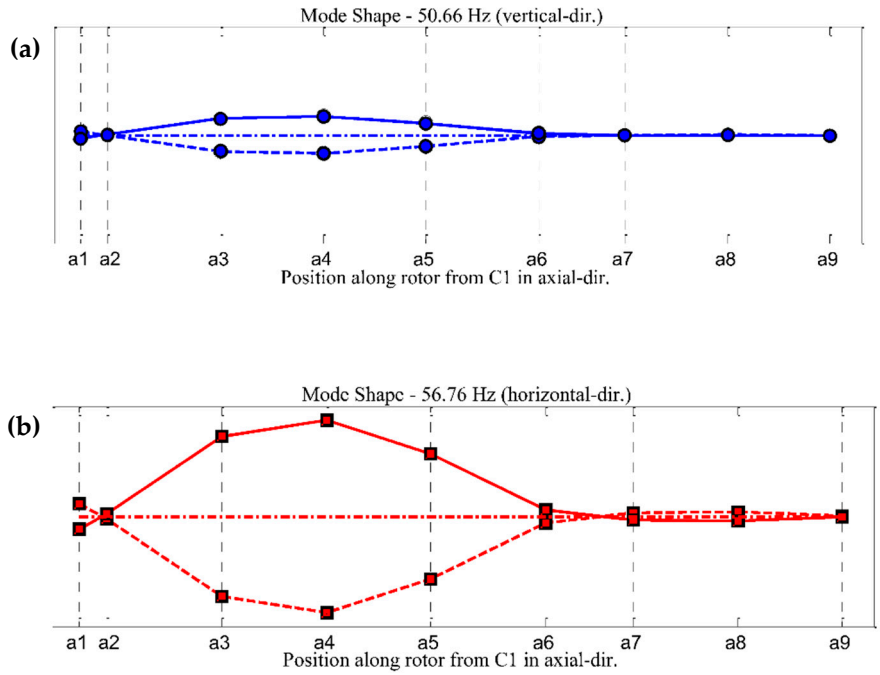

Figure 2. Experimental mode shapes: (**a**) 50.66 Hz, vertical direction dominant; (**b**) 56.76 Hz, horizontal direction dominant [20].

2.2. Experimental Data

In the experimental development of the vibration-based machine-learning (VML) model, a random number of samples are used from five rotor conditions and two operational speeds [21]. The healthy condition and 4 different rotor-related faults, i.e., misalignment, shaft bow, looseness in bearing pedestal, and rotor rub, are included. These faults were independently introduced to the rig. The vibration samples were collected at a sampling frequency of 10 ksamples per second, simultaneously obtaining the measurements at the 4 bearing cases along the rig. The data were acquired from the rig operating at 1800 RPM (30 Hz) and 2400 RPM (40 Hz).

Vibration data from the healthy condition are subject of residual misalignment and residual unbalance, as expected, with predominant peak at 1x frequency order. For reference, the velocity spectra of the faulty conditions at 1800 RPM are shown in Figure 3a–d.

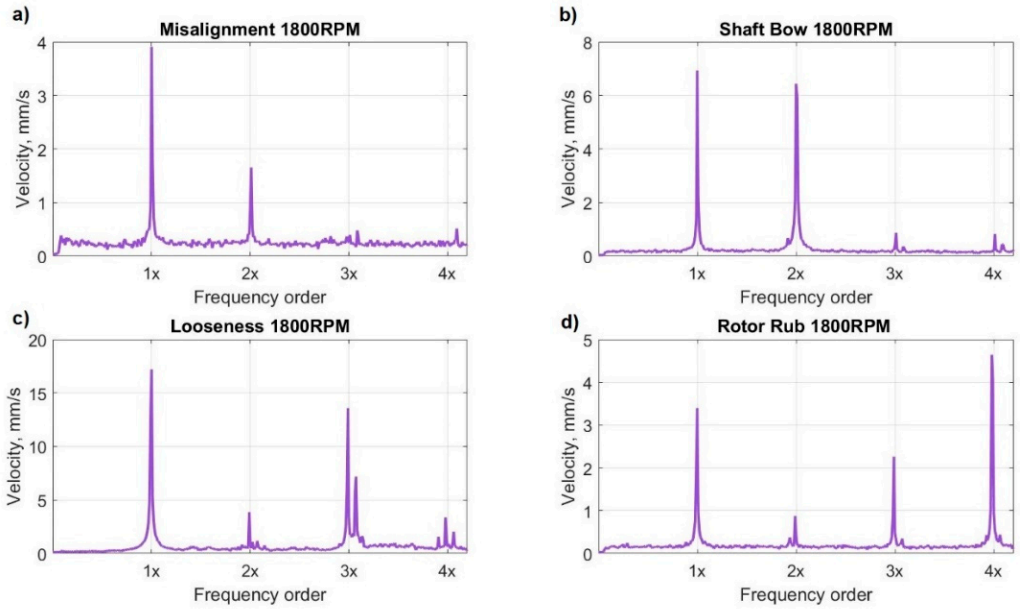

Figure 3. Typical experimental velocity spectrum plots from data at 1800 RPM, at B3 location. (**a**) Misalignment; (**b**) Shaft bow; (**c**) Looseness in pedestal; (**d**) Rotor rub.

3. Optimised Experimental Model [21]

3.1. Vibration-Based Machine-Learning Model for the Fault Diagnosis in Rotating Machines

The VML fault diagnosis model [22] was developed using an artificial neural network (ANN). The defined ANN is a multilayer perceptron (MLP), which has an input layer, 4 hidden layers, and an output layer with 5 possible classes as diagnoses, related to the 5 rotor conditions. The hidden layers have a variable number of nonlinear neurons—1000 100, 100, and 10 neurons respectively, from layers 1 to 4. The number of layers and neurons were adjusted by iterations to obtain the desired performance in the fault diagnosis [22]. These layers are illustrated in Figure 4, where the schematic of the implemented MLP is presented. The transfer function set at hidden neurons is the hyperbolic tangent sigmoid [23] and at output layers is the SoftMax [24]; the scaled conjugate gradient backpropagation is the selected training function along to the cross-entropy, which is the performance function.

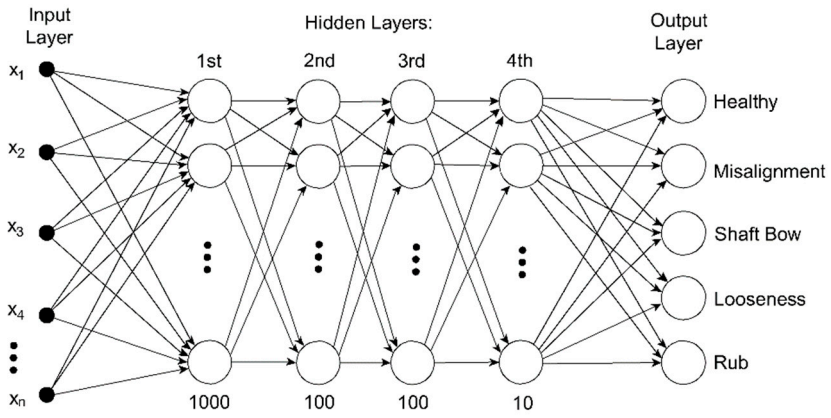

Figure 4. Multilayer perceptron neural network.

The inputs of the network are built by the optimised parameters from the acceleration signals in time domain and velocity in frequency domain [21]. From time domain, the calculated features are root mean square (RMS) and kurtosis (K). From the frequency domain,

the amplitudes of the velocity spectra at 1×, 2×, 3× and the spectrum energy (SE) between 0.5 Hz and 500 Hz are included. Each $input_i$ contains these parameters from the 4 bearing locations as per Equation (1).

$$input_i = [RMS1_i \ K1_i \ 1x1_i \ 2x1_i \ 3x1_i \ SE1_i \ RMS2_i \dots SE2_i \ RMS3_i \dots SE3_i \ RMS4_i \dots SE4_i]^T \quad (1)$$

The available samples are grouped into 70%–15%–15% for training, validation, and testing, respectively. The performance of the model is calculated as per Equation (2).

$$\%Performance(or\ \%Diagnosis) = \frac{No.correct\ classifications}{total\ inputs} * 100\% \quad (2)$$

3.2. Results of Experimental Optimised Model

The results obtained in the VML fault diagnosis model using the optimised parameters are listed in Table 1. The model trained with data only collected at 1800 RPM is blindly tested with data collected at 2400 RPM, providing excellent results in the blind application. The separation between healthy and faulty samples reaches 100% accuracy, while the performance on the diagnosis of the exact rotor fault is just under 100%. These promising results will be further validated in this paper using vibration data simulated in the FE model of the experimental rig.

Table 1. Blind application performance (%) at 2400 RPM of the proposed VML model.

Actual / Diagnosis	Healthy	Misalignment	Bow	Looseness	Rub
Healthy	100.0	0.0	0.0	0.0	0.0
Misalignment	0.0	100.0	0.0	0.0	0.0
Bow	0.0	0.0	100.0	0.0	0.0
Looseness	0.0	0.0	0.0	98.9	0.0
Rub	0.0	0.0	0.0	1.1	100.0

4. Finite-Element Model and Vibration Responses Estimation

Aiming at understanding the dynamics of the experimental rig, as well to validate the VML fault diagnosis model earlier developed, a finite-element (FE) model of the studied machine is developed. The FE model developed earlier [25] is further updated to reflect the experimental rig dynamics. This method allows the representation of complex rotor systems. The 5 studied rotor conditions listed in Table 1 are then simulated independently in the FE model. This FE model is used to generate vibration responses similar to the experiments for the 5 conditions. Mathematical approaches, such as FE method, allow the simulation of vibration responses under different fault types, sizes, and locations, which is an exorbitant and time-consuming process when it is conducted experimentally.

4.1. An FE Model and Mode Shapes

The rig is analysed by a shaft-line model. The structure (Sh1, C2, Sh2) is divided into 150 2-node Timoshenko beam elements, with a total of 151 nodes in the model. The components of the rig, such as flexible coupling, balancing discs, bearings, and pedestals, are represented by their dynamic characteristics as concentrated masses at their location nodes. The schematic of this representation is shown in Figure 5.

The well-known Timoshenko beam theory [26] is implemented to develop the central equation of motion of the system. Four generalised coordinates are defined at each $i-node$ for the lateral vibrations, i.e., u_i, v_i, θ_i, ψ_i, where u_i and v_i are translations and θ_i and ψ_i are rotations. The effects of shear and rotary inertia are included in the calculations. Since there are not clear and defined physical parameters for damping as per mass and stiff-

ness, in structural mechanics it is normally considered low enough to be neglected, or simplified models are implemented, such as proportional damping [27]. In this model, the damping is updated using the proportional damping approach.

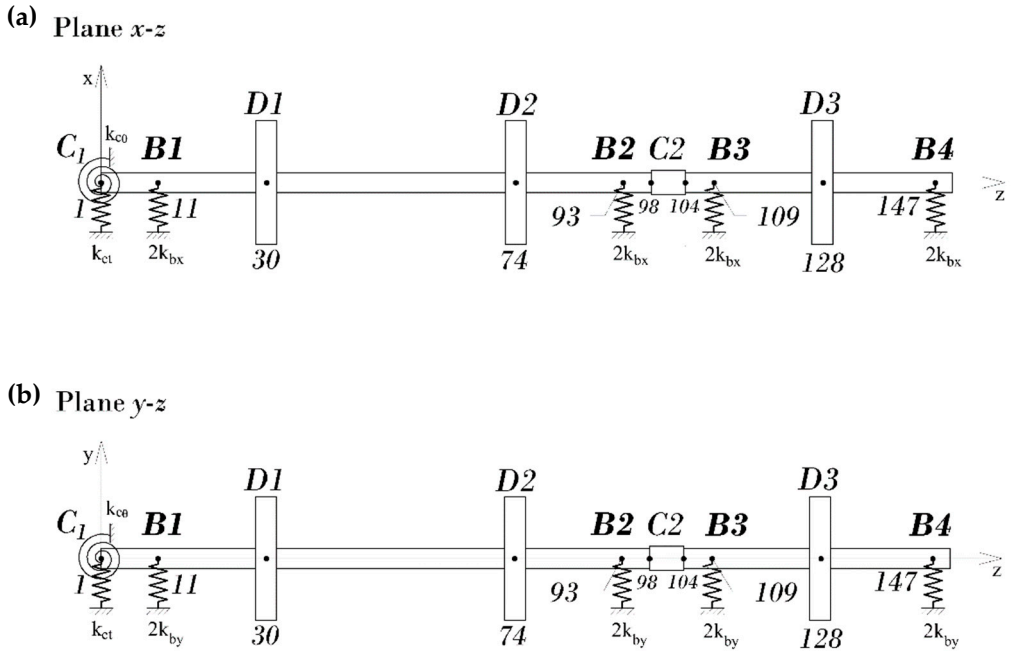

Figure 5. Schematic of FE simulation of the experimental rig. (**a**) Plane x–z. (**b**) Plane y–z.

The elements of the rig are added in the model as follows:

- Flexible coupling, C1: the flexible coupling between the rotor and the motor is used to remove the motor vibration influence on the rotor to maximum extent. Therefore, the coupling mass and stiffnesses are only added to Node 1 of the FE model to account the dynamics related to the rotor.
- Rigid coupling, C2: this element is modeled using the Timoshenko beam theory, as it is considered a rigid link in the central shaft-line model.
- Balancing discs, D1, D2, D3: the mass and gyroscopic matrices of the discs are added to Nodes 30, 74, and 128, respectively.
- Bearings and their pedestals: the mass and equivalent stiffnesses are added to respective Nodes, 11, 93, 109, and 147. The stiffness values at these locations are determined by iterations until the first and second natural frequencies known from the experimentally identified natural frequencies are matched.

The equation of motion is assembled with all the described elements, resulting in Equation (3), where $\mathbf{M}$ is the mass matrix; $\mathbf{C}$ is the damping matrix; $\mathbf{G}$ is the gyroscopic matrix dependent on the rotating speed Ω; and $\boldsymbol{K}$ is the stiffness matrix. The mass and stiffness proportional damping matrix, $\mathbf{C}$, is determined based on the proportional coefficients using the experimentally obtained modal damping. $\mathbf{F}(t)$ represents the forces, such as unbalance and other external forces, that could be applied to the system. $\boldsymbol{q}(t)$ is the response vector. The studied rotor conditions are then added to the equation of the system, Equation (3), by modifications of the stiffness matrix and/or adding external forces, depending on the simulated defect.

$$\mathbf{M}\ddot{\boldsymbol{q}}(t) + (\mathbf{C} + \Omega\mathbf{G})\dot{\boldsymbol{q}}(t) + \boldsymbol{K}\boldsymbol{q}(t) = \boldsymbol{F}(t) \quad (3)$$

The first and second natural frequencies obtained in the FE model are listed in Table 2, where they are compared to the natural frequencies known from the experimental

modal test of the rig [20]. The mode shapes corresponding to these natural frequencies are shown in Figure 6.

Table 2. Experimental and mathematical natural frequencies of studied rig.

Natural Frequency	Experimental, Hz	Mathematical, Hz	Error (%)	Dominant Direction
f_{n1}	50.6600	50.6650	+0.010	Y-direction
f_{n2}	56.7600	56.7625	+0.004	X-direction

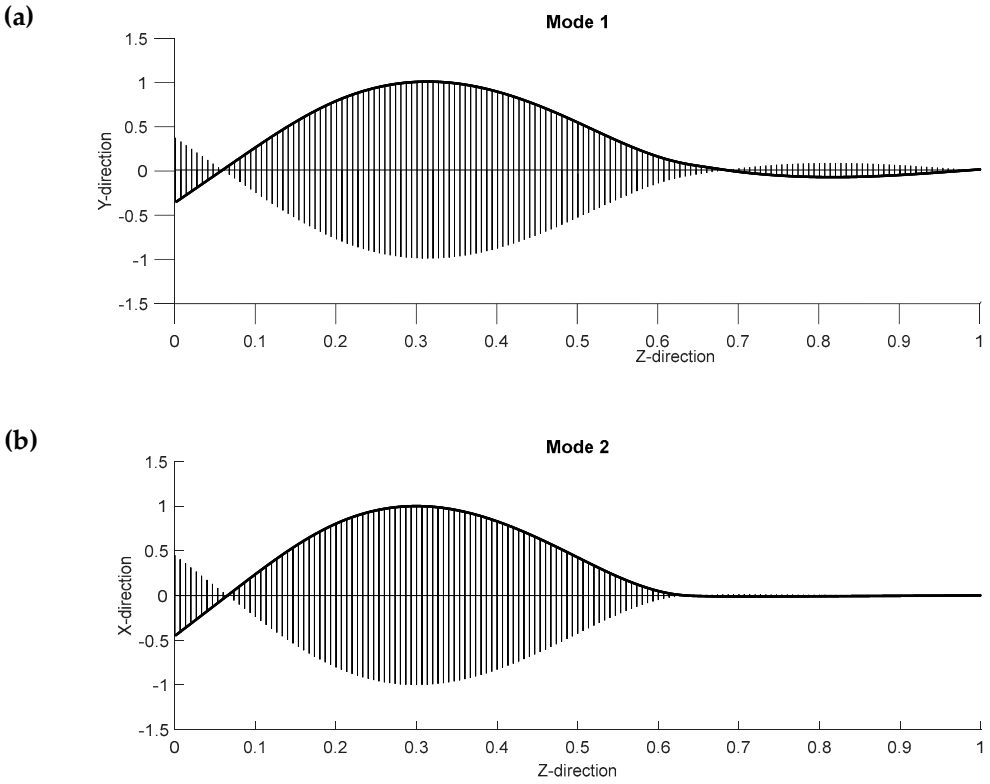

Figure 6. First and second mode shapes simulated in the FE model developed. (**a**) First natural frequency 50.66 Hz; dominant in the Y-direction. (**b**) Second natural frequency 56.76 Hz; dominant in the X-direction.

4.2. Rotor Conditions Simulation

Using the updated FE model representing the experimental rig, the vibration acceleration responses are estimated for each rotor condition similar to the experiments. Details of each rotor condition simulation are discussed in the following sections.

4.2.1. Healthy Rotor (Residual Unbalance)

The simulation of the healthy machine condition is conducted by adding the effects of residual unbalance. The effects of residual misalignment observed in the experimental rig are not included in this FE model. The residual unbalance force, F_u, arises in the system when the mass centerline differs from the equilibrium position during the machine operation. In this model, the residual unbalance is considered to exist at D3 location (Node 128), with an eccentricity of $\varepsilon = 0.93\,mm$. The phase angle, α, is randomly changed to

simulate different starts of the machine; this way several data are generated for the studied healthy and faulty conditions. The time-dependent force is added to the system, modifying Equation (3) as [28]

$$\mathbf{M}\ddot{\boldsymbol{q}}(t) + \Omega\mathbf{G}\dot{\boldsymbol{q}}(t) + \mathbf{C}\dot{\boldsymbol{q}}(\mathrm{t}) + \boldsymbol{K}\boldsymbol{q}(t) = \Re\left(\Omega^2\boldsymbol{b}_{\boldsymbol{0e}}e^{(j\Omega t+\alpha)}\right) \quad (4)$$

where the force, $\Re\left(\Omega^2\boldsymbol{b}_{\boldsymbol{0e}}e^{j(\Omega t+\alpha)}\right)$ is the unbalance force at an angle of α.

4.2.2. Misalignment

As with the experiments, a parallel misalignment in introduced to the FE model. The vertical offset of 0.8 mm is considered to exist at bearing 1, B1, location. There is no offset considered to occur in the horizontal direction. The forces and moments in the flexible coupling, C1, regarding this misalignment are estimated adapting the general case of reaction forces calculation developed by Gibbons [29]. The equation of the forced response of the system includes both the residual unbalance and misalignment forces. Misalignment forces, $\Re(\boldsymbol{F_m}e^{j\Omega t} + \boldsymbol{F_m}e^{j2\Omega t})$, are considered to appear periodically at 1× and 2× in the frequency spectrum, while other higher harmonics regarding them are neglected. The equation of motion, Equation (3), is now written as

$$\mathbf{M}\ddot{\boldsymbol{q}}(t) + \Omega\mathbf{G}\dot{\boldsymbol{q}}(t) + \mathbf{C}\dot{\boldsymbol{q}}(t) + \boldsymbol{K}\boldsymbol{q}(t) = \Re\left(\Omega^2\boldsymbol{b}_{\boldsymbol{0e}}e^{(j\Omega t+\alpha)}\right) + \Re(\boldsymbol{F_m}e^{j\Omega t} + \boldsymbol{F_m}e^{j2\Omega t}) \quad (5)$$

4.2.3. Shaft Bow

The simulation of bent shaft is carried out by considering a known deflection of the longest shaft of the rig, Sh1, between bearings 1 (B1) and bearing 2 (B2). The shape of this deflection is assumed to be a parabolic curve as shown in Figure 7. The forces are calculated in a similar way to the unbalance forces [28], by considering a variable eccentricity along the shaft, $\varepsilon(z)$, which is determined as a function of the axial position, z. The maximum deformation is assumed at the centre of the shaft and equal to 4.0 mm. The theoretical response obtained by this simulation will only show the unbalance at 1× in the spectrum. Thus, in order to distinguish the bow condition from the healthy condition, a very small residual misalignment is also added to this fault. The residual misalignment force, $\Re(\boldsymbol{F_{Rm}}e^{j\Omega t} + \boldsymbol{F_{Rm}}e^{j2\Omega t})$, is calculated as per Section 4.2.2.

Figure 7. Schematic of defection assumed at shaft 1, Sh1, in shaft bow simulation.

The governing equation of the system, Equation (3), is updated into Equation (6), which includes the residual unbalance and residual misalignment forces, along to the forces due bow condition ($\boldsymbol{K}\boldsymbol{q}_{\boldsymbol{B}}$).

$$\boldsymbol{M}\ddot{\boldsymbol{q}}(t) + (\Omega\boldsymbol{G} + \boldsymbol{C})\dot{\boldsymbol{q}}(t) + \boldsymbol{K}\boldsymbol{q}(t) = \boldsymbol{K}\boldsymbol{q}_{\boldsymbol{B}} + \Re\left(\Omega^2\boldsymbol{b}_{\boldsymbol{0e}}e^{(j\Omega t+\alpha)}\right) + \Re(\boldsymbol{F_{Rm}}e^{j\Omega t} + \boldsymbol{F_{Rm}}e^{j2\Omega t}) \quad (6)$$

4.2.4. Looseness in Bearing Pedestal

The looseness in the FE model is simulated at pedestal 3, P3, location. It is assumed that all bolts at P3 are loosened and that their axis are coincident with the vertical direction of the general coordinates. The clearance within the surface, δ_L, may allow a restricted displacement in the vertical direction, depending on the direction of the unbalance forces acting during the rotor operation. Any possible small displacements in the horizontal direction are considered to be negligible.

The stiffness at the loosened location is modified according to the vertical position of the rotor. Three possibilities are identified, which determine the changes in stiffness values and the addition of external forces to the equation of motion of the system. The definition of these values in sections provides a nonlinear vibration system with piecewise linear parameters [30]. The static equilibrium position is at $y = 0$, with the rotor resting on the surface. The supports are considered to have an elastic behaviour.

In Equation (7) the 3 possible vertical positions, $y < 0$; $0 \le y \le \delta_L$; $y > \delta_L$, are defined. In these expressions, k_{vs3} represents the variable vertical stiffness and f_{Lvs3} represents the variable vertical force, both due the loosened support at P3 location; k_b is the vertical stiffness value of the non-loosened support.

$$\begin{matrix} y < 0 \begin{cases} k_{vs3} = k_b \\ f_{Lvs3} = 0 \end{cases} \\ 0 \le y \le \delta_L \begin{cases} k_{vs3} = 0 \\ f_{Lvs3} = 0 \end{cases} \\ y > 0 \begin{cases} k_{vs3} = k_b \\ f_{Lvs3} = k_b \delta_L \end{cases} \end{matrix} \quad (7)$$

As $\boldsymbol{K_0}$ is the stiffness matrix of the system without the loosened support contribution and $\boldsymbol{K_s}$ the matrix containing the variable stiffness due looseness in pedestal 3, the equation of motion, Equation (3), can be written as Equation (8), where $\boldsymbol{K_s q_c}$ is the force $\boldsymbol{F_L}$ due the loosened pedestal. This expression now includes the residual unbalance forces and looseness effects.

$$\boldsymbol{M}\ddot{\boldsymbol{q}}(t) + (\Omega \boldsymbol{G} + \boldsymbol{C})\dot{\boldsymbol{q}}(t) + (\boldsymbol{K_0} + \boldsymbol{K_s})\boldsymbol{q}(t) = \Re\left(\Omega^2 \boldsymbol{b_{0e}} e^{(j\Omega t + \alpha)}\right) + \boldsymbol{K_s q_c} \quad (8)$$

4.2.5. Rotor Rub

To address the simulation of rub between a rotating and a stationary part, it is considered that the impact generates a modification in the dynamic characteristics of the rotor [31]. Partial rub of the rotor is assumed to exist with a static surface located in the positive vertical direction. A clearance, δ_R, is assumed to exist between both parts when the rotor is at its resting position. The contact is introduced at Node 39, near the balancing disc 1, D1, similarly to the experiments. When contact occurs, the rotor is subject of 2 forces; the normal force f_n in the negative vertical direction and its respective friction force $f_t = \mu_k \cdot f_n$, where μ_k is the kinetic friction coefficient.

Similar to the mechanical looseness simulation, it is considered a variable stiffness depending on the position of the rotor during operation due residual unbalance effect. In this case, there are two possibilities at Node 39:

1. the displacement is lower or equal than the defined clearance δ_R in the vertical direction and free motion is observed in the rotor, then the equation of motion remains as Equation (4);
2. displacement is higher than the clearance δ_R and contact exists between rotor and stator, increasing the stiffness due the stator effect. A high value of stator stiffness is defined, and the equation of motion is updated following the same considerations than in the looseness model, obtaining Equation (9). In this equation, $\boldsymbol{K_{st}}$ represents the increment on stiffness and $\boldsymbol{F_R}$ the forces, both due the contact.

$$\ddot{\boldsymbol{q}}(t) + (\Omega \boldsymbol{G} + \boldsymbol{C})\dot{\boldsymbol{q}}(t) + (\boldsymbol{K} + \boldsymbol{K_{st}})\boldsymbol{q}(t) = \Re\left(\Omega^2 \boldsymbol{b_{0e}} e^{(j\Omega t + \alpha)}\right) + \boldsymbol{F_R} \quad (9)$$

4.3. Responses Estimation

The Newmark-β method [32] is used to solve the governing equation for each rotor condition to estimate the responses at the measurement locations. The steady-state acceleration vibration responses at the bearing B1 to B4 are estimated at two rotor speeds, namely 1800 RPM (30 Hz) and 2400 RPM (40 Hz), similar to the experiments. The vibration

acceleration responses data at bearings B1 to B4 for the rig when running for 5 s are considered to be 1 sample. Therefore, the number of samples generated from the FE model for each rotor condition are exactly same as the experimental samples. The time interval, $\Delta t = 10^{-4}$ s is used in the Newmark-β method to keep the identical sampling frequency of 10 kHz used in the experimental data. Likewise, each sample generated from the FE model has a length of 5 s, similar to the experiments. The random unbalance phase angle was used in the FE model for each rotor condition to estimate each sample of responses. This approach reflects the random starting point in the vibration measurements. Finally, the random noise with a signal-to-noise ratio (SNR) of 30 dB is added to each generated response (i.e., each sample) to simulate the measurement noises.

Typical velocity spectra at the bearing B3 calculated from the estimated responses for the simulated faulty conditions are shown in Figure 8. These spectra are similar but not identical to the experimental spectra (Figure 3) of the rig. The difference can be understood due to the assumptions taken into account to simulate the defects, such as neglecting the effect of residual misalignment in 3 of the 4 faulty rotor conditions. However, the exact responses are not attempted here but the FE model is considered good enough for the purpose to validate the optimised parameters and the VML fault diagnosis model earlier developed [21].

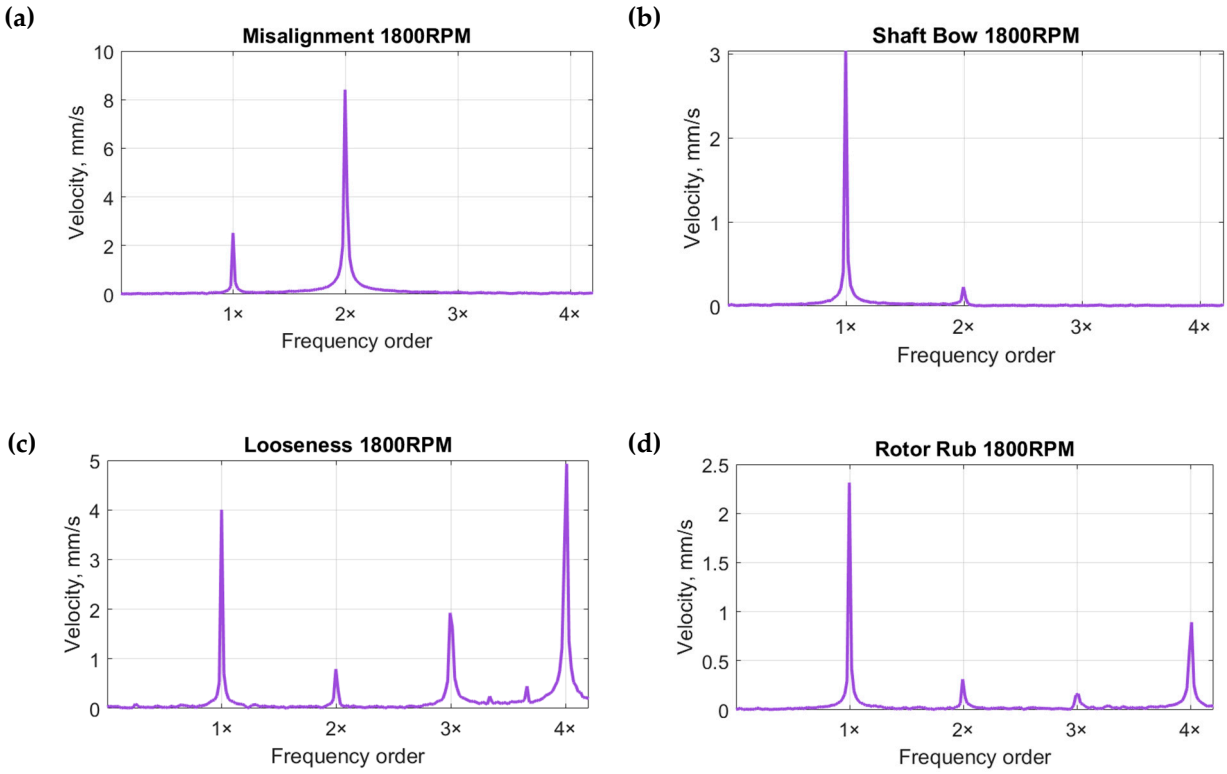

Figure 8. Velocity spectrum plots from data generated in the FE model at 1800 RPM, at B3 location. (**a**) Misalignment; (**b**) Shaft bow; (**c**) Looseness in pedestal; (**d**) Rotor rub.

5. Mathematical Validation

The validation of the experimentally optimised features is conducted using the vibration signals simulated in the FE model for the studied rotor conditions. The number of samples used per rotor condition and speed is identical to the experimental study [21].

The validation is conducted first with data only at 1800 RPM, and then the blind application at 2400 RPM is carried out. In both cases, the inputs of the network are built using Equation (1). The RMS and kurtosis from time domain, and 1×, 2×, 3× amplitudes

from velocity spectra along to spectrum energy between 0.5 Hz and 500 Hz are calculated from the estimated responses to populate the inputs as Equation (1).

5.1. Validation at 1800 RPM

The exact steps described in Section 3 used in the experimental model are applied again to the simulated data. First, only data generated at the speed of 1800 RPM is used to generate the inputs of the network as per Equation (1). The available data were randomly divided into 70% for training, 15% for validation, and 15% for testing. The obtained performances at the different stages of the learning and testing processes are determined as per Equation (2). The results are shown in Figure 9. The obtained results show 100% accuracy in the separation of faulty from healthy samples. All the samples for each rotor fault condition are correctly identified with 100% of accuracy. These results are completely in agreement with the experimental observations [21].

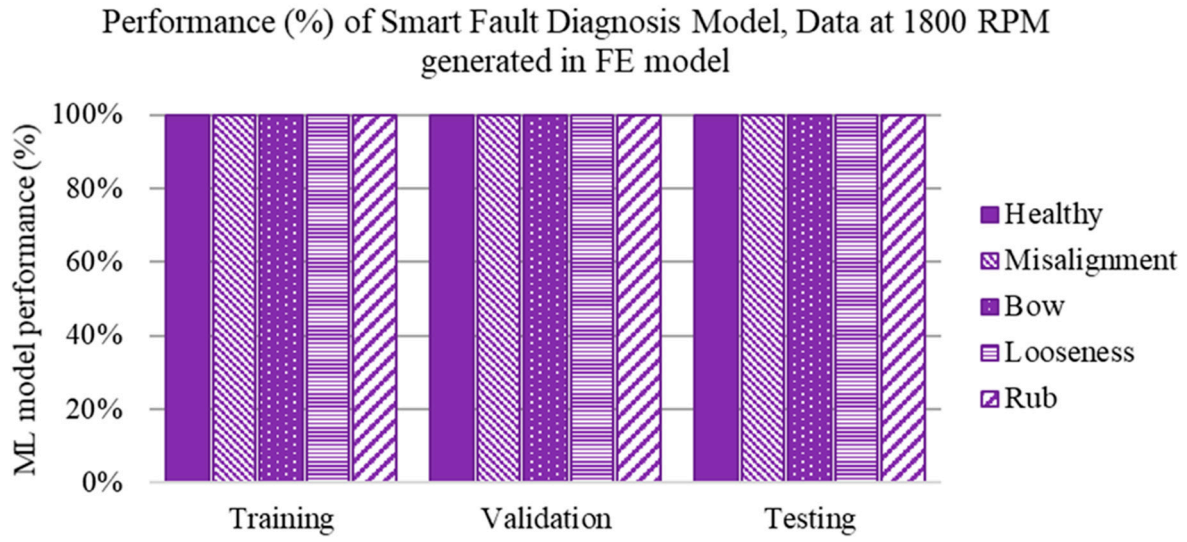

Figure 9. Performance (%) of VML fault diagnosis model, using only data generated at 1800 RPM in the FE model.

5.2. Validation of Blind Application

After training the VML fault diagnosis model with vibration data generated in the FE model only at 1800 RPM, the validation of its blind application is carried out for the simulated data at the machine speed of 2400 RPM. For this, the already-trained model is now tested with data samples generated at a different machine speed, i.e., 2400 RPM. The results obtained in the blind test are listed in Table 3. In Figure 10, the results obtained in the validation run, using data from the FE model, are compared against the performances obtained through experimental data. The results suggest that the selected parameters provide a correct characterisation of the dynamics of the studied rotor conditions. This allows the delivery of an accurate diagnosis on the machine even when there are no data available to train the model at the required speed.

The healthy condition and the 4 faults are correctly identified both experimentally and mathematically. This validates both the parameters used and the VML model, and their robustness. A little error in the diagnosis of the looseness fault in the experimental model as the misalignment should be acceptable. This may be due to an early stage of looseness. However, the model is still separating with a 100% of accuracy the faulty samples from the healthy ones. These are promising results that provide a real possibility for industrial application. The proposed smart model is capable of providing reliable diagnoses even when the operational speed is slightly changed.

Table 3. Performance (%) obtained in blind test of VML fault detection model, using data generated at 2400 RPM in the FE model.

Actual / Diagnosis	Healthy	Misalignment	Bow	Looseness	Rub
Healthy	100.0	0.0	0.0	0.0	0.0
Misalignment	0.0	100.0	0.0	0.0	0.0
Bow	0.0	0.0	100.0	0.0	0.0
Looseness	0.0	0.0	0.0	100.0	0.0
Rub	0.0	0.0	0.0	0.0	100.0

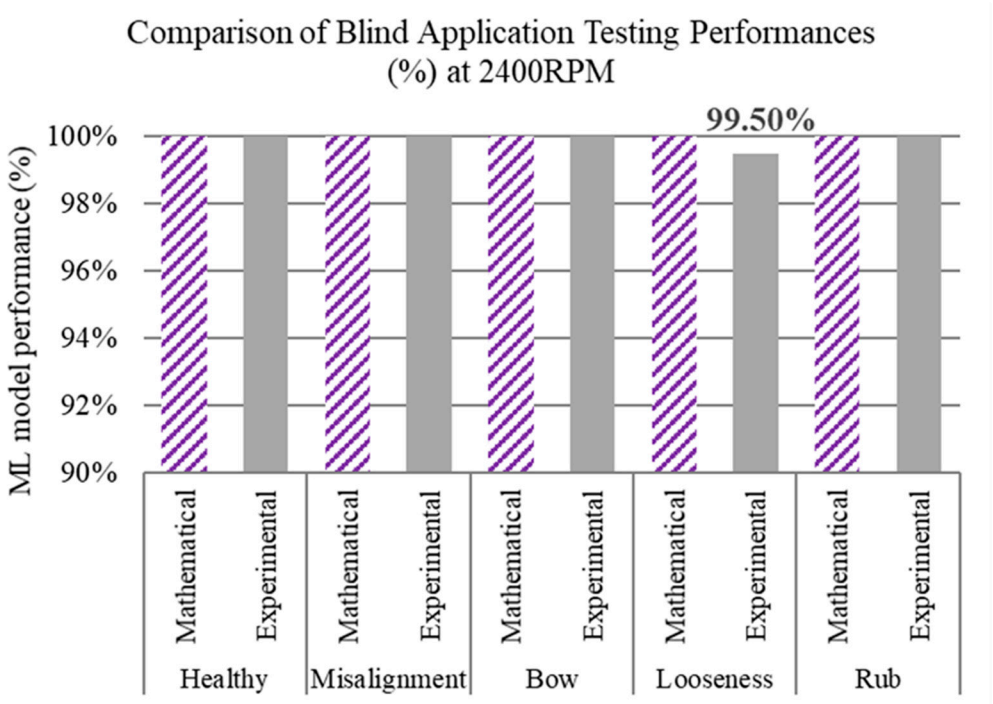

Figure 10. Comparison of performance (%) using experimental data and data generated in the FE model in the blind application of VML fault detection model at 2400 RPM.

6. Concluding Remarks

In this paper, a FE model of an experimental rig has been developed. Then, the estimated vibration responses are used to conduct the validation of the optimised parameters of the VML fault diagnosis model earlier developed. The validation through FE-simulated responses considers the same rotor faults, the same number of samples, and the same speeds included on the former study based on experimental data. The validation is carried out following the exact same steps followed in the experimental study, using identical ANN architecture and parameters to populate the inputs of the network.

The dynamics of the experimental rig are represented through the FE-based mathematical simulation, for both the healthy and faulty conditions, which includes 4 different rotor-related defects. From the simulated vibration responses, the data used in the model validation are obtained. The conducted validation confirms the correctness of the selected parameters, from both time and frequency domains, to characterise and distinguish the different faults in the rotor.

An accurate prediction in the exact fault type even in the blind application is observed. This makes the model reliable for being used at different speeds, which becomes very important in industrial applications, as historical data at the required operational speed may not be available to train a machine-learning model.

These promising results provide a real possibility for industrial application, where further faults could be included, such as motor faults and bearing related defects. Furthermore, the FE model can be used to extend the scope of the VML fault diagnosis model, by allowing the inclusion of new rotor faults, as well different sizes and locations, avoiding the time-consuming and extensive work related to experimental fault simulations.

Author Contributions: N.E.S.: concept and all data analysis, J.S.: concept and supervision model. All authors have read and agreed to the published version of the manuscript.

Funding: This research received no external funding

Acknowledgments: Natalia Fernanda Espinoza Sepúlveda acknowledges the support by CONICYT (Comisión Nacional de Investigación Científica y Tecnológica/Chilean National Commission for Scientific and Technological Research) "Becas Chile" Doctorate's Fellowship programme; Grant No2190062 for her PhD study.

Conflicts of Interest: The authors declare no conflict of interest. The funders had no role in the design of the study; in the collection, analyses, or interpretation of data; in the writing of the manuscript, or in the decision to publish the results.

References

1. Thiery, F.; Aidanpää, J.O. Nonlinear vibrations of a misaligned bladed Jeffcott rotor. *Nonlinear Dyn*. **2016**, 86, 1807–1821.
2. Vlajic, N.; Champneys, A.R.; Balachandran, B. Nonlinear dynamics of a Jeffcott rotor with torsional deformations and rotor-stator contact. Int. *J. Non. Linear. Mech.* **2017**, *92*, 102–110.
3. Chávez, J.P.; Hamaneh, V.V.; Wiercigroch, M. Modelling and experimental verification of an asymmetric Jeffcott rotor with radial clearance. *J. Sound Vib.* **2015**, *334*, 86–97.
4. Guo, C.; Al-Shudeifat, M.A.; Yan, J.; Bergman, L.A.; McFarland, D.M.; Butcher, E.A. Application of empirical mode decomposition to a Jeffcott rotor with a breathing crack, *J. Sound Vib.* **2013**, *332*, 3881–3892.
5. Guo, C.; Yan, J.; Yang, W. Crack detection for a Jeffcott rotor with a transverse crack: An experimental investigation. *Mech. Syst. Signal Process.* **2017**, *83*, 260–271.
6. Gómez, M.J.; Castejón, C. Crack detection in rotating shafts based on 3× energy: Analytical and experimental analyses. *MAMT.* **2016**, *96*, 94–106.
7. Singh, S.; Tiwari, R. Model-based switching-crack identification in a Jeffcott rotor with an offset disk integrated with an active magnetic bearing. *J. Dyn. Syst. Meas. Control. Trans. ASME*. **2016**, *138*, 031006.
8. Heindel, S.; Becker, F.; and Rinderknecht, S. Unbalance and resonance elimination with active bearings on a Jeffcott Rotor. *Mech. Syst. Signal Process*. **2017**, *85*, 339–353.
9. Eissa, M.; Saeed, N.A. Nonlinear vibration control of a horizontally supported Jeffcott-rotor system. *JVC/Journal Vib. Control*. **2018**, *24*, 5898–5921.
10. Chen, G. Simulation of casing vibration resulting from blade-casing rubbing and its verifications. *J. Sound Vib.* **2016**, *361*, 190–209.
11. Hong, J.; Li, T.; Liang, Z.; Zhang, D.;Ma, Y. Research on blade-casing rub-impact mechanism by experiment and simulation in aeroengines. *Shock Vib*. **2019**, *2019*, 3237960.
12. Wang, N.; Liu, C.; Jiang, D. Prediction of transient vibration response of dual-rotor-blade-casing system with blade off. *Proc. Inst. Mech. Eng. Part G J. Aerosp. Eng*. **2019**, *233*, 5164–5176.
13. Guo, X.; Zeng, J.; Ma, H.; Zhao, C.;Yu, X.; Wen, B. A dynamic model for simulating rubbing between blade and flexible casing. *J. Sound Vib*. **2019**, *466*, 115036.
14. Zeng, J.; Ma, H.; Yu, K.; Guo, X.; Wen, B. Rubbing response comparisons between single blade and flexible ring using different rubbing force models. *Int. J. Mech. Sci*. **2019**, *164*, 105164.
15. Mokhtar, M.A.; Darpe, A.K.; Gupta, K. Analysis of stator vibration response for the diagnosis of rub in a coupled rotor-stator system. *Int. J. Mech*. Sci. **2018**, *144*, 392–406.
16. Xiang, L.; Gao, X.; Hu, A. Nonlinear dynamics of an asymmetric rotor-bearing system with coupling faults of crack and rub-impact under oil-film forces. *Nonlinear Dyn*. **2016**, *86*, 1057–1067.
17. Xiang, L.; Deng, Z.; Hu, A.; Gao, X. Multi-fault coupling study of a rotor system in experimental and numerical analyses. *Nonlinear Dyn*. **2019**, *97*, 2607–2625.
18. Xiang, L.; Zhang, Y.; Hu, A. Crack characteristic analysis of multi-fault rotor system based on whirl orbits. *Nonlinear Dyn*. **2019**, *95*, 2675–2690.
19. Wang, S.; Zi, Y.; Qian, S.; Zi, B.; Bi, C. Effects of unbalance on the nonlinear dynamics of rotors with transverse cracks. *Nonlinear Dyn*. **2018**, *91*, 2755–2772.
20. Nembhard, A.D.; Sinha, J.K.; Yunusa-Kaltungo, A. Experimental observations in the shaft orbits of relatively flexible machines with different rotor related faults. *Measurement*. **2015**, *75*, 320–337.

21. Espinoza Sepulveda, N.F.; Sinha, J.K. Parameter optimisation in the vibration-based machine learning model for accurate and reliable faults diagnosis in rotating machines. *Machines*. **2020**, *8*, 66.
22. Espinoza Sepulveda, N.; Sinha, J.K. Blind application of developed smart vibration-based machine learning (SVML) model for machine faults diagnosis to different machine conditions. *J. Vib. Eng. Technol*. **2020**, *9*, 587–596.
23. Vogl, T.P.; Mangis, J.K.; Rigler, A.K.; Zink,W.T.; Alkon, D.L. Accelerating the convergence of the backpropagation method. *Biol. Cybern*. **1988**, *59*, 257–263.
24. Bishop, C.M. *Pattern Recognition and Machine Learning*; Springer: New York, NY, USA, 2006.
25. Espinoza Sepulveda, N.F.; Sinha, J.K. Theoretical validation of experimental rotor fault detection model previously developed. In Mechanisms and Machine Science, 105. In *Proceedings of the IncoME-V & CEPE Net-2020, Beijing Institute of Technology, Zhuhai, China, 23–25 October 2020*; Springer: Cham, Switzerland, 2021; pp. 169–177.
26. Timoshenko, S.P. LXVI. On the correction for shear of the differential equation for transverse vibrations of prismatic bars. *London Edinburgh Dublin Philos. Mag. J. Sci*. **1921**, *41*, 744–746.
27. Friswell, M.I.; Mottershead, J.E. *Finite Element Model Updating in Structural Dynamics*; Kluwer Academic Publishers: Dordrecht, The Netherlands, 1995.
28. Friswell, M.; Penny, J.; Garvey, S.; Lees, A. *Dynamics of Rotating Machines*, 1st ed.; Cambridge University Press: Cambridge, UK, 2010.
29. Gibbons, C.B.B. Coupling misalignment forces. In *Proceedings of the 5th Turbomachinery Symposium*; Texas A&M University, Gas Turbine Laboratories: Texas, USA, 1976, pp. 111–116.
30. Chu, F.; Tang, Y. Stability and non-linear responses of a rotor-bearing system with pedestal looseness. *J. Sound Vib.* **2001**, *241*, 879–893.
31. Goldman, P.; Muszynska, A.; Chaotic behavior of rotor/stator systems with rubs. *ASME. J. Eng. Gas Turbines Power*. **1994**, *116*, 692–701.
32. Rao, S.S. *Mechanical Vibrations*, 3rd ed.; Addison-Wesley: Reading, MA, USA, 1995.